crystals

MDPI

Article

Effect of the Composition of the Ceramics (MCeMgSr)$O_{2-\delta}$ (M = Y, Sm) on the Microstructure, Mechanical and Electrical Properties for Solid Electrolyte

Irina Vasilevna Sudzhanskaya [1,*], Yulia Sergeevna Nekrasova [2] and Alexander Sergeevich Kubankin [1]

[1] Belgorod National Research University, 85, Pobedy Str., 308015 Belgorod, Russia
[2] Belgorod State Technological University Named after V.G. Shukhov, 46, Kostyukova Str., 308012 Belgorod, Russia
* Correspondence: sudzhanskaya@bsu.edu.ru; Tel.: +7-910-369-5112

Abstract: The samples of ceramics (Y,Ce,Mg,Sr)$O_{2-\delta}$; 10YCe3Mg5Sr; 10SmCe3Mg5Sr were obtained by the method of standard solid-state reaction. According to X-ray analysis, all systems have the fluorite cubic structure, but in the (Y,Ce,Mg,Sr)$O_{2-\delta}$ system, the presence of the second orthorhombic phase was observed. The microstructure of powders and synthesized tablets were characterized by electron-microscopy. The average particle size of the powder was shown to be 23.88 nm; 22.32 nm; and 13.4 nm for the compositions (Y,Ce,Mg,Sr)$O_{2-\delta}$; 10YCe3Mg5Sr; and 10SmCe3Mg5Sr, respectively. After the sintering at temperature 1450 °C; the grain size increased to 5.1 μm; 3.95 μm; 5.07 μm for (Y,Ce,Mg,Sr)$O_{2-\delta}$; 10YCe5Mg5Sr; and 10SmCe5Mg5Sr, respectively. The ionic conduction of the obtained samples was defined by ac impedance spectroscopy. The activation energy was then calculated. The 10SmCe5Mg5Sr system was found to have the highest electrical conductivity, reaching 20.5 mS/cm at a temperature of 700 °C. The activation energy was 0.62 eV in the temperature range of 600–800 °C. The results of the density, microhardness, and crack resistance measurements of the solid solutions under investigation were obtained.

Keywords: multicomponent oxide; ionic conductivity; impedance spectroscopy; solid electrolyte

Citation: Sudzhanskaya, I.V.; Nekrasova, Y.S.; Kubankin, A.S. Effect of the Composition of the Ceramics (MCeMgSr)$O_{2-\delta}$ (M = Y, Sm) on the Microstructure, Mechanical and Electrical Properties for Solid Electrolyte. *Crystals* **2022**, *12*, 1198. https://doi.org/10.3390/cryst12091198

Academic Editor: Maria Gazda

Received: 28 June 2022
Accepted: 23 August 2022
Published: 25 August 2022

1. Introduction

Solid oxide fuel cells (SOFCs) convert chemical fuel energy into electrical energy in an environmentally friendly way with a cogeneration efficiency of approximately 60–85% [1–4]. The ceramic materials on the base of ZrO_2, stabilized Y, Sc, Ca, etc., are the most popular among the wide spectra of materials for the production of the solid electrolyte in the high-temperature range. However, the disadvantage for practical application of SOFCs is high operating temperatures (800–1000 °C), at which the conductivity of the main component–the solid electrolyte—reaches a sufficient level. At high temperatures, the degradation processes and chemical interaction of SOFCs components are accelerated, and the problem of compatibility of thermal properties of materials arises, which is the reason for the high cost of SOFCs and limits their commercialization [5–8].

The application of the cerium with fluorite structure, doped by the rare earth and alkaline metals for the production of solid electrolytes of the solid oxide fuel cell, leads to the decrease in the operating temperature to 500 °C–800 °C (ITSOFC) [9–18]. Moreover, the solid electrolytes based on cerium dioxide have an order of magnitude greater electric conductivity (~10^{-1}–10^{-2} S/cm) than zirconium dioxide in the intermediate temperature [19–22], which is due to the large ionic radius of the Ce^{4+} cation (0.96 Å) compared to Zr^{4+} (0.84 Å) [21], resulting in a crystal structure with large conduction channels [23]. However, the main disadvantage of the doped electrolytes based on the dioxide of cerium application is significant electronic conductivity, especially at intermediate temperatures, which causes a partial internal electrical short-circuiting in the cell [24–26]. To find a

solution to the arising problem, scientists concentrated on the conception of the polycomponent doping of electrolytes based on cerium with the fluorite structure using two approaches: the first is the manufacturing of the high-entropy oxides (HEOs) with 20–25% concentration of cerium dioxide [27–29]. The second approach is the manufacturing of the multicomponent dioxide ceramics with the concentration of the cerium oxide being no more than 80% [14,23,30–34].

In the first approach, the highly-entropic oxide systems (Ce, Gd, Nd, Pr, Sm, Mox) $O_{2-\delta}$ and (Ce, Gd, La, Nd, Pr, Mox) $O_{2-\delta}$, x = 0, 0.3, 0.5 were obtained by the authors of [27]. It was found that the conductivity activation energy of obtained ceramic systems in the temperature range 25–450 °C is 0.55–0.59 eV. Evidently, the samples have a sufficiently high electrical conductivity at low temperatures because of the predominance of the electron type of conductivity due to the jumps of electrons (polarons) associated mainly with Pr^{3+}/Pr^{4+} ions. In the temperature range 500–1000 °C, the conductivity activation energy of obtained systems is 0.64–0.69 eV, respectively.

The second approach is the manufacturing of the multicomponent oxide ceramics with the concentration of the cerium oxide being no more than 80% [14,23,30–35].

In addition to rare earth metals (Sm, Gd, Y), it is cost-effective to use alkaline earth oxides, such as MgO, SrO, as dopants of cerium dioxide [23,32–42]. They create additional oxygen vacancies, thereby reducing the activation energy and improving the conductivity of the oxide ions at intermediate temperatures.

Y. Zheng, L. Wu [39] showed that co-doping of CeO_2 with yttrium and strontium leads to an ionic conductivity improvement at a temperature 750 °C by two times compared with doping only with Y. Co-doping of Sm_2O_3 and MgO improves the electrical characteristics of the cerium-based electrolytes. The materials' cost for producing the ceria-based intermediate temperature solid oxide fuel cells (IT-SOFCs) may be significantly reduced owing to the cost difference between Mg and Sm [40].

Co-doping of the cerium dioxide by Sm, Sr was studied in [23,41,42]. It was found [23] that $Ce_{0.78}Sm_{0.20}Sr_{0.02}O_{1.88}$ has a high ionic conductivity compared with $Ce_{0.8}Sm_{0.2}O_{1.9}$. These authors ascribed the enhancement in the conductivity to the increase in the number of oxygen vacancies, decrease in the association enthalpy, and increase in radius of oxygen vacancies, which widened the channels for easy movement of oxygen ions. Oxides of alkaline earth metals are not less profitable than oxides of rare earth metals.

The feature of the use of alkaline earth metals as alloying additives is not only the creation of the additional oxygen vacancies but also the scavenging of siliceous impurities present at the grain boundaries, which leads to an increase in the grain boundaries' conductivity and, in turn, the total conductivity of the electrolyte.

The authors of [34] studied the scavenging effect of MgO. It reacts with SiO_2 and the resultant material gathers at the triple point junction of the grain boundaries; as a result, the resistance of the grain boundaries is reduced. The scavenging effect of SrO has been studied in the works [42,43].

An example of a two-fold increase in electrical conductivity of the solid electrolyte $Ce_{0.8}Sm_{0.2}O_{1.9}$ by doping with Sr is given in [42]. The authors substantiate an increase in electrical conductivity of $Ce_{0.82}Sm_{0.16}Sr_{0.02}$ $O_{1.90}$ composition with a scavenging effect of Sr.

The objective of this work was to compare the electrical and mechanical properties of the multicomponent systems with high entropy $Y_{0.25}Ce_{0.25}Mg_{0.25}Sr_{0.25}O_{2-\delta}$, multicomponent systems based on the cerium dioxide (~80%) $Y_{0.1}Ce_{0.78}Mg_{0.03}Sr_{0.05}O_{2-\delta}$, $Sm_{0.1}Ce_{0.78}Mg_{0.03}S$ $_{0.05}O_{2-\delta}$.

2. Materials and Methods

The samples of $Y_{0.25}Ce_{0.25}Mg_{0.25}Sr_{0.25}O_{2-\delta}$, (Y,Ce,Mg,Sr)$O_{2-\delta}$, $Y_{0.1}Ce_{0.82}Mg_{0.03}Sr_{0.05}O_{2-\delta}$ (10YCe3Mg5Sr), and $Sm_{0.1}Ce_{0.82}Mg_{0.03}Sr_{0.05}O_{2-\delta}$ (10SmCe3Mg5Sr) compositions were synthesized by solid-state reaction from precursors: $Ce(NO_3)_3 \bullet 6H_2O$, 99.9%, $Sr(CO_3)_2$, Y_2O_3 и $MgCO_3$, $(Sm(NO_3)_3 \bullet 6H_2O)_3$, 99.9% (Sigma Aldrich), taken in stoichiometric ratio.

The powders of $Ce(NO_3)_3 \bullet 6H_2O$, $MgCO_3$, $(Sm(NO_3)_3 \bullet 6H_2O$ were annealed at 600 °C for 30 min until the formation of CeO_2, Mg_2O_3, and Sm_2O_3. The obtention of the oxide phase was determined by the X-ray method. The powder was ground in an agate mortar for 2 h with the addition of ethyl alcohol, then dried. The synthesized mixture was compressed in form of discs with a diameter of 10 mm and a height of 1 mm by the method of isostatic pressing at a pressure of 250 MPa. The samples were sintered in an air atmosphere at 1450 °C for 4 h. After sintering, the samples were thoroughly ground and polished for further study of the formed structure and properties.

The phase composition of the ceramics was investigated by X-ray phase analysis on the diffractometer Rigaku Ultima IV. The particle size of the synthesized powders was determined based on the transmission electron microscope (TEM) JEM 2100 (Japanese Electron Optics Laboratory, Jeol) images. The microstructure of the obtained ceramic pellets was studied using the the scanning electronic microscope (SEM) Quanta 600 FEG (FEI, Netherlands), and their elemental composition was determined through energy dispersive spectroscopy (EDS). Density was measured by micrometrics AccuPyc II 1340 helium pycnometer. There were 15 measurements taken for every sample. The average value was recorded as the result.

Relative density (ρ) was determined as a ratio of the apparent density (ρ_{exp}) to the theoretical density (ρ_{th}) according to the dependence (1).

$$\rho = (\rho_{exp} / \rho_{th}) \times 100\% \quad (1)$$

The theoretical density was calculated from the following crystallographic Equation (2) [44]:

$$\rho_{th} = (Z \sum_I v_i M_i)/(a^3 Na) \quad (2)$$

where Z is the number of formula units per unit cell (i.e., 4 for the fluorite structure of ceria), v_i is the stoichiometric coefficient of the element i, M_i is the molar mass in g × mol^{-1}, a is the lattice parameter from XRD patterns (Table 1), and N_a is Avogadro's number, equal 6022 × 10^{23} mol^{-1}.

Table 1. The results of the apparent and relative densities, microhardness, and crack resistance measurements of the ceramics $(Y,Ce,Mg,Sr)O_{2-\delta}$, 10YCe3Mg5Sr, and 10SmCe3Mg5Sr.

S. No	Compositions	Apparent Density, g/sm^3	Relative Density, %	Vickers Hardness, Hv, GPa	Crack Resistance, $MPam^{1/2}$
1	$(Y,Ce,Mg,Sr)O_{2-\delta}$	4.4	88	7.26	1.48
2	10YCe3Mg5Sr	6.0	90	7.80	1.82
3	10SmCe3Mg5Sr	6.48	96	7.80	2.1

DM-8 microhardness meter was used to measure the Vickers microhardness and crack resistance. Load on the indenter was 0.1 kg, introduction time of the indenter into the material surface was 15 s. The total number of prints made on the sample surface was 10.

The crack resistance (K_{1c} ($MPam^{1/2}$)) of material was defined using Niihara's Formula (3) [45]:

$$K_{1c} = 0.203 (c/a)^{-3/2} H a^{1/2} \quad (3)$$

Here, a is a length of diagonal of the indenter print (mm), c is a crack length (mm), and H–Vickers hardness (H_v).

The electric properties of the ceramics were investigated using Novocontrol concept 43 impedance, equipped with platinum contacts, at a heating rate of 0.3 K/min within a temperature ranging from 300 K to 1070 K and frequency ranging from 10^{-2} Hz to 10^7 Hz. To measure the impedance, a sample in the form of pellets was used with a diameter of 10 mm and a thickness of 1.0 mm; both sides of the sample were coated with silver paste electrodes.

3. Results

The samples of ceramics (Y,Ce,Mg,Sr)$O_{2-\delta}$, 10YCe3Mg5Sr, and 10SmCe3Mg5Sr were sintered at a temperature of 1450 °C. The results of microindentation, as well as the values of density measured by picnometry, are presented in Table 1. It was found that the ceramics system 10SmCe3Mg5Sr had the largest density, which is 6.48 g/cm^3 (96%), and the ceramic (Y,Ce,Mg,Sr)$O_{2-\delta}$, had the smallest density, which is 4.4 g/cm^3 (88%) and corresponds to the microscopy results presented below. The obtained SEM-images demonstrate the dense structure and the smallest number of pores in the 10SmCe3Mg5Sr system. The results of microhardness and crack resistance measurements range from 7.26 to 7.8 GPa and 1.48–2.2 MPam$^{1/2}$, are in agreement with the results presented in [13,37,46] for $Ce_{0.8}M_{0.2}O_{2-\delta}$ (M = Y, Sm, Gd, La Nd) systems, and are also compared with the crack resistance of the pure CeO_2, which is 1.5 MPam$^{1/2}$ [47].

3.1. XRD Analysis

The diffractograms of the sintered ceramic samples of (Y,Ce,Mg,Sr)$O_{2-\delta}$, 10YCe3Mg5Sr, and 10SmCe3Mg5Sr compositions showing that the cubic structure of fluorite, belonging to CeO_2 with space group of symmetry $Fm\bar{3}m$ (225), according to the reference pattern for this oxide (ICDD, PDF 00-043-1002) and crystal lattice parameters, given in Table 2, prevails in all systems. These are presented in Figure 1a.

Table 2. Phase content data, average grain size, and lattice parameter of composition of the sintered ceramics.

S. No	Compositions	Average Grain Size 1450 °C (μm)	Phase Content Data	Lattice Parameter (Å)
1	(Y,Ce,Mg,Sr)$O_{2-\delta}$	5.1	Fm3m	5.3944
			Pnam	10.1086, 11.9452, 3.4275
2	10YCe3Mg5Sr	3.95	Fm3m	5.4142
3	10SmCe3Mg5Sr	5.07	Fm3m	5.4426

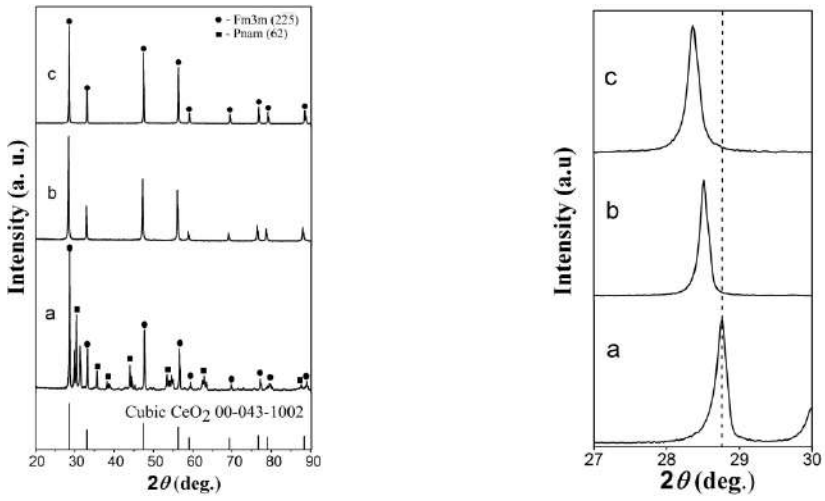

Figure 1. (**a**) X-ray diffractograms of the sintered ceramics (a) (Y,Ce,Mg,Sr)$O_{2-\delta}$, (b) 10YCe3Mg5Sr, and (c) 10SmCe3Mg5Sr. Reported in the International Centre for Diffraction Data (ICDD) XRD patterns corresponding to the cubic CeO_2; (**b**) shift in the peak position for (111) peak.

However, in the (Y,Ce,Mg,Sr)$O_{2-\delta}$ system, the presence of the second orthorhombic phase with the symmetry space group Pnam (62), corresponding to SrY_2O_4 and amounting to approximately 33%, is observed, which is due to the poor solubility of Sr^{2+} and Y^{3+} (5–10%) in the cerium oxide lattice [48].

An increase occurred in the lattice parameter (Table 2) in the system of electrolyte 10SmCe3Mg5Sr, connected with the large ion radius of Sm^{3+} (1.08 Å) [23,42] in comparison with Y^{3+} (0.90 Å) [49]. An increase in the lattice parameter was additionally confirmed by the peak intensity decreasing and its shifting towards low values of 2θ with the composition changing (Figure 1b).

The ionic conduction of the dioxide cerium multicomponent electrolytes depends on the oxygen vacancies' radius. The large radius of an oxygen vacancy creates a wide channel for ion conductivity that increases it [23,31,50], and this is confirmed by the results of electric conductivity measurements presented below.

3.2. TEM Aanalysis

TEM-images of 10SmCe3Mg5Sr, 10YCe3Mg5Sr, and $(Y,Ce,Mg,Sr)O_{2-\delta}$ powders are shown in Figure 2. The obtained compositions 10SmCe3Mg5Sr and 10YCe3Mg5Sr have rounded grains (Figure 2a,b). In the powder $(Y,Ce,Mg,Sr)O_{2-\delta}$, rounded grains predominate in larger amounts and grains with a crystal cut in small amounts (Figure 2c). Each individual powder showed a uniform particle size distribution in the nanometer range. However, the average particle size in $(Y,Ce,Mg,Sr)O_{2-\delta}$ and 10SmCe3Mg5Sr compositions decreased from 23.88 nm to 13.4 nm. The largest grain size dispersion from 9.55 nm to 56.9 nm in $(Y,Ce,Mg,Sr)O_{2-\delta}$ powder was observed. The composition of 10YCe3Mg5Sr powder was most uniform by the grain size. The average grain size was 22.32 nm, min–12.16 nm, max–35.08 nm. The composition of 10SmCe3Mg5Sr powder had the least grain size, with a minimal value of 6.57 nm and a maximum value of 25.9 nm.

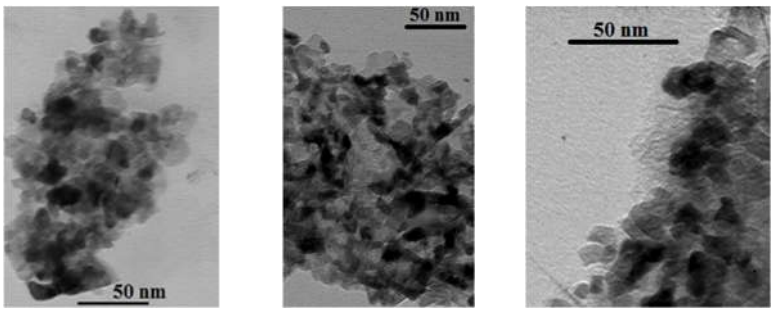

(**a**) (**b**) (**c**)

Figure 2. TEM images of powders (**a**) 10SmCe3Mg5Sr; (**b**) 10YCe3Mg5Sr; and (**c**) $(Y,Ce,Mg,Sr)O_{2-\delta}$.

The crystallite sizes of powders obtained by TEM method (d) are in agreement with the XRD analysis results, and were calculated by the Scherrer Equation (4):

$$d = k\lambda/\beta\cos\theta \quad (4)$$

where d is the crystallite size, k is the shape factor (=0.9), λ is the wavelength of radiation, β is the full width half maxima of the (111) plane of reflection, and θ is the diffraction angle.

The calculated crystallite sizes are: 13.8 nm for 10SmCe3Mg5Sr; 11.9 nm for 10YCe3Mg5Sr; the $(Y,Ce,Mg,Sr)O_{2-\delta}$ contains two phases, 20.3 nm corresponds to the cubic phase belonging to CeO_2, and 58.7 nm corresponds to the orthorhombic phase SrY_2O_4.

3.3. Microstructure

SEM images of the cleavage of sintered samples of 10SmCe3Mg5Sr, 10YCe3Mg5Sr, and $(Y,Ce,Mg,Sr)O_{2-\delta}$ ceramics at a temperature of 1450 °C are presented in Figure 3.

Grains of a rounded form with the average size of 5.1 μm were observed in the $(Y,Ce,Mg,Sr)O_{2-\delta}$ ceramic system (Figure 3a). In the samples of 10YCe3Mg5Sr and 10SmCe3Mg5Sr ceramics (Figure 3b,c), grains with a crystal cut and an average size of 3.95 μm and 5.07 μm, respectively, prevailed, on the boundaries of which there were spheres, as shown in Figure 3d on the example of the 10SmCe3Mg5Sr system sample, associated with grain boundaries scavenging effect and with a decrease of resistance on the grain boundaries [41,43,51].

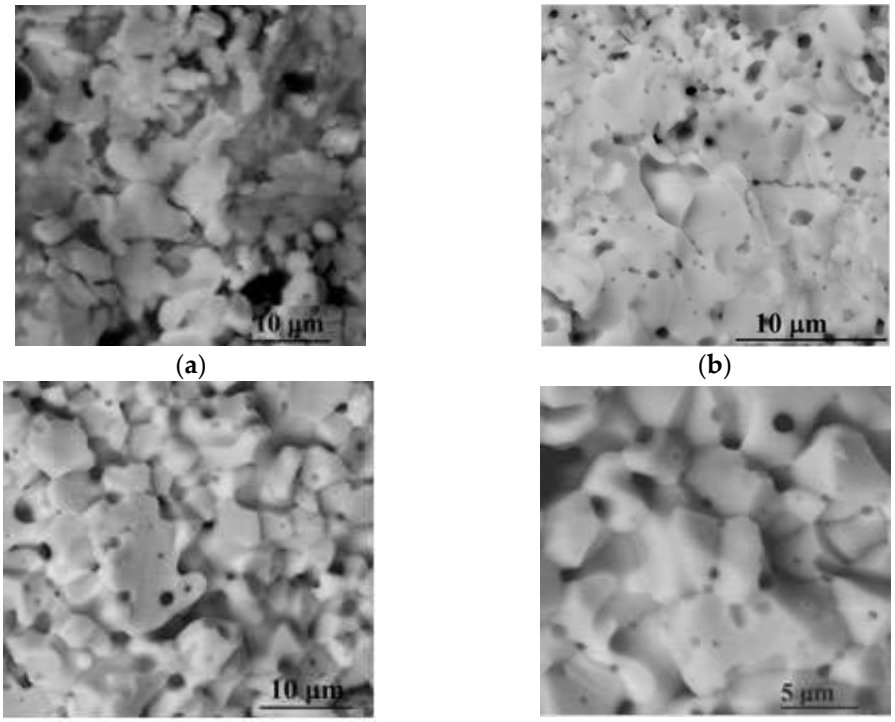

(**a**) (**b**)

(**c**) (**d**)

Figure 3. SEM images of the slices of the ceramic materials (**a**) (Y,Ce,Mg,Sr)$O_{2-\delta}$; (**b**) 10YCe3Mg5Sr; and (**c**,**d**) 10SmCe3Mg5Sr.

The elemental analysis of the sintered ceramics was performed using EDS. The EDS results, along with the elemental mapping of 10YCe3Mg5Sr and 10SmCe3Mg5Sr, are shown in Figure 4. The weight percentages of all the compositions are shown in Table 3.

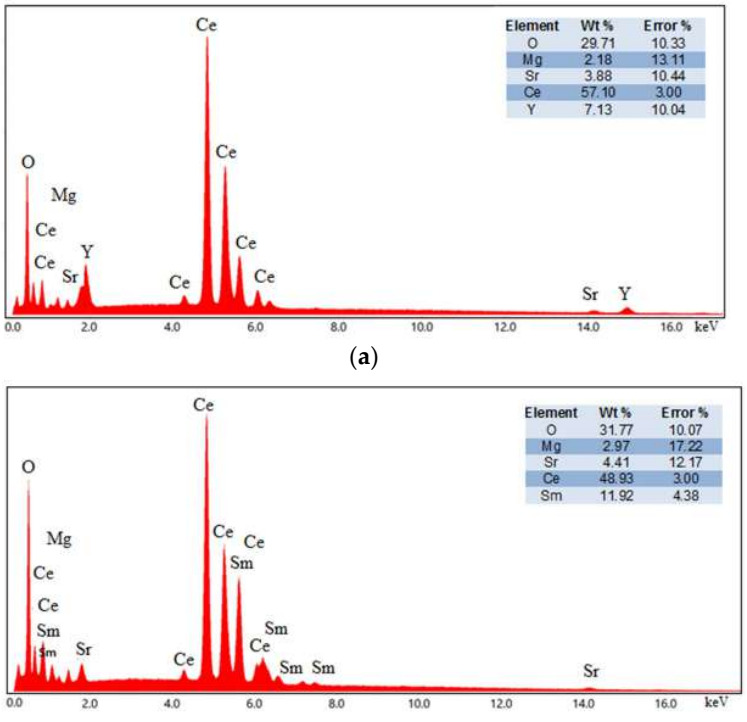

(**a**)

(**b**)

Figure 4. EDS spectrograph of (**a**) 10YCe3Mg5Sr and (**b**) 10SmCe3Mg5Sr sintered ceramic pellets.

Table 3. Weight % obtained from EDS analysis of the sintered ceramics.

Composition	Element	Weight % from EDS	Error %
$(Y,Ce,Mg,Sr)O_{2-\delta}$	O	6.47	2.39
	Mg	17.04	1.12
	Sr	23.28	0.61
	Ce	25.31	0.6
	Y	27.90	0.43
10YCe3Mg5Sr	O	29.71	10.33
	Mg	2.18	13.11
	Sr	3.88	10.44
	Ce	57.10	3.00
	Y	7.13	10.04
10SmCe3Mg5Sr	O	31.77	10.07
	Mg	2.97	17.22
	Sr	4.41	12.17
	Ce	48.93	3.00
	Sm	11.92	4.38

Obtained spectrograms and maps confirm the presence and homogeneous distribution of all elements in the sintered electrolyte pellets.

3.4. Electric Conductivity

Doped cerium oxide in the air atmosphere has ionic conductivity that is carried out by the migration of oxygen vacancies [19]. The Nyquist graphs for all three systems obtained at a temperature of 415 K are shown in Figure 5.

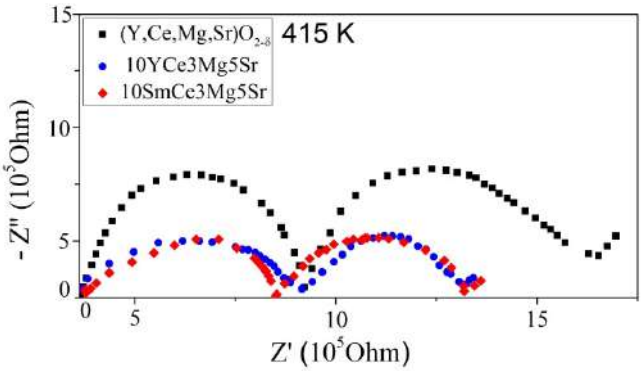

Figure 5. The impedance spectra of $(Y,Ce,Mg,Sr)O_{2-\delta}$, 10YCe3Mg5Sr, and 10SmCe3Mg5Sr ceramics, constructed in Nyquist coordinates at a temperature 415 K.

The impedance spectra analysis and the selection of equivalent circuits were carried out in the framework of the block model [52]. The choice of impedance temperature is defined by a possibility to estimate the contribution of the volume of grains and the grain boundaries to the total resistance. Since with increasing temperature, the relaxation frequency of all polarization processes increases, it leads to a shift of the corresponding arcs to the region of higher frequencies. Due to the limited frequency range available in the equipment, all of these arcs cannot be observed.

On the graph of each of the samples in the measured frequency range two semicircles are observed, indicating the presence of two relaxing processes: the high-frequency arc

describes polarization in the grain and the middle-frequency arc is connected with polarization on the grain boundary. In this case, the third section corresponds to the influence of the electrodes, and it is not taken into account at all. The inset in Figure 4 shows the equivalent circuits, containing included in series two parallel-connected sub-circuits with an element of the constant phase (CPE = Q), bulk resistance (R_b), and grain boundary resistance (R_{gb}). An element of the constant phase is used to describe the resistive-capacitive properties of the system in an equivalent electrical circuit, since the microstructure of the samples is inhomogeneous. The total resistance (R_t) is defined by the following dependence: $R_t = R_b + R_{gb}$. Ionic conductivity is expressed by the formula: $\sigma = t/(R \times A)$, where σ (S/cm)–ionic conductivity, R (Ohm)–total resistance, A (cm^2)–the surface tablet area, and t–the tablet thickness.

It is evident from Figure 4 that the system (Y,Ce,Mg,Sr)$O_{2-\delta}$ has the largest resistance with indistinctly expressed arcs, corresponding to the bulk resistance and grain boundary resistance. The increase in the resistance of HEO (Y,Ce,Mg,Sr)$O_{2-\delta}$ in comparison with the systems 10YCe3Mg5Sr and 10SmCe3Mg5Sr is due to the fact that for the cerium oxide, the upper doping limit exists above a certain upper limit, and the concentration of the alloying substance leads to an increase in defects (oxygen vacancies) [53,54]. It reduces the electrolyte conductivity as the defects begin to interact with each other; as a result, the oxygen vacancies' mobility decreases, and therefore, so does the conductivity. The obtained HEO (Y,Ce,Mg,Sr)$O_{2-\delta}$ has a higher doping level, as a result of which the conductivity decreases and the resistance increases.

Temperature dependences of the total (σ_t), bulk (σ_b), and grain boundary (σ_{gb}) conductivities of the (Y,Ce,Mg,Sr)$O_{2-\delta}$, 10YCe3Mg5Sr, and 10SmCe3Mg5Sr systems, the graphs of which are given in Figure 6a,b in coordinates lnσ (1/T), obey the Arrhenius law (5):

$$\sigma = \sigma_0 \exp(-E/kT) \quad (5)$$

where σ_0–prefactor; E–the energy of the electrical conductivity activation; and k–Boltzmann constant, equal to 1.38×10^{-23} J/K.

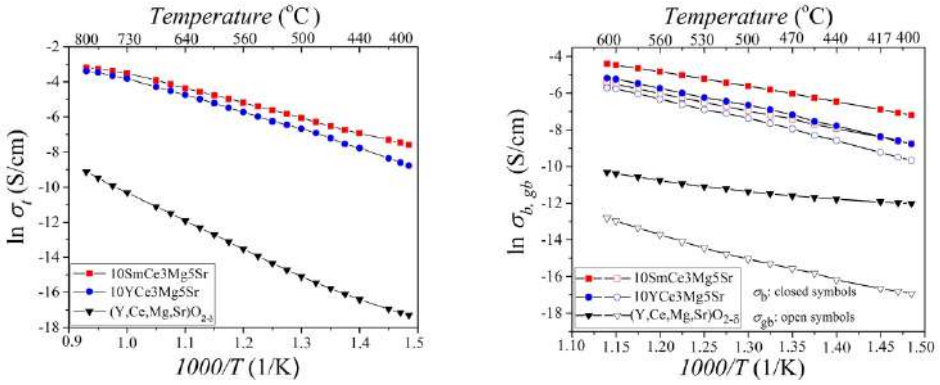

(**a**) (**b**)

Figure 6. Temperature dependence of (**a**) the total, (**b**) the bulk, and the grain boundary electrical conductivity for 10SmCe3Mg5Sr, 10YCe3Mg5Sr, and (Y,Ce,Mg,Sr)$O_{2-\delta}$ ceramics in Arrhenius coordinates. Closed symbols correspond to the bulk conductivity, opened symbols to the grain boundary conductivity.

The analysis of the electric conductivity temperature dependence of the obtained systems indicates an increase of conductivity in all samples with a temperature increase, which is associated with the destruction of defect associates while releasing more and more mobile charge carriers, which leads to an increase of ionic conductivity. To explain the charge carriers' mobility at different temperatures, the activation energy of the conductivity process was calculated by the slope of the dependence lnσ at 1000/T. The values of the electric conductivity and activation energy are presented in Table 4. At a low-temperature

range (400–600 °C), the activation energy of the ceramics 10YCe3Mg5Sr and 10SmCe3Mg5Sr is more than at an intermediate temperature range (600–800 °C), since at a low-temperature range, the activation energy is necessary for the destruction of defect associates and release of mobile charge carriers, as well as for the migration of oxygen vacancies. On the other hand, in the high-temperature range, the activation energy is consumed only for the migration of oxygen vacancies [41,43,55].

Table 4. The values of the total electrical conductivity and of the activation energy of the total, bulk, and grain boundary conductivity of ceramics 10SmCe3Mg5Sr, 10YCe3Mg5Sr, and (Y,Ce,Mg,Sr)$O_{2-\delta}$ at various temperatures.

S. No	Materials	σ_t, S/cm		E_t, eV				E_b, eV			E_{gb}, eV		
		500 °C	700 °C	400–600 °C	600–800 °C	400–470 °C	470–800 °C	400–600 °C	400–470 °C	470–600 °C	400–600 °C	400–470 °C	470–600 °C
1	(Y,Ce,Mg,Sr)$O_{2-\delta}$	3.12×10^{-7}	2.1×10^{-5}	-	-	0.96	1.37	-	0.3	0.6	-	0.96	1.17
2	10YCe3Mg5Sr	1.38×10^{-3}	1.7×10^{-2}	0.90	0.72	-	-	0.89	-	-	1.0	-	-
3	10SmCe3Mg5Sr	1.7×10^{-3}	2.05×10^{-2}	0.72	0.62	-	-	0.70	-	-	0.82	-	-

However, the activation energy of the total conductivity of HEO (Y,Ce,Mg,Sr)$O_{2-\delta}$ increases with the temperature increasing from 0.96 eV (400–470 °C) to 1.37 eV (470–800 °C), due to the prevailing of the electronic type of conductivity at a given temperature range. This effect is more clearly observed in the characteristic temperature dependence of the electrical conductivity of the bulk in the Arrhenius coordinates, shown in Figure 6b, according to which the activation energy increases with increasing temperature from 0.3 eV (400–470 °C) to 0.6 eV (470–600 °C).

According to the Arrhenius graph shown in Figure 6b, the bulk conductivity is larger than the grain boundary conductivity for all systems. The activation energy of the grain boundary conductivity is higher than the activation energy of the bulk conductivity, which is consistent with the results of the work presented in [24,35,41,43].

Among the received ceramics with a concentration of CeO_2 ~80%, the lowest activation energy (E_a = 0.62 eV) and the highest value of ionic conductivity (σ_{700} = 20.5 mS/cm) were found in the system 10SmCe3Mg5Sr, since the ionic radius Sm^{3+} (1.08 Å) was larger than Y^{3+} (0.9 Å), which provides a larger channel of the oxygen-ionic conductivity [23,53].

HEO (Y,Ce,Mg,Sr)$O_{2-\delta}$ had the highest activation energy and the lowest electrical conductivity due to the presence of a second orthorhombic phase SrY_2O_4, which has dielectric properties with a band gap of 4.9 eV [55].

The obtained investigation results of the multicomponent system 10SmCe5Mg5Sr match with the results of the authors' other works. Thus, for example, in [56], at 700 °C the electrical conductivity of a system 20ErDC was 18.22 mS/cm, Et (400–600 °C) = 0.97 eV, Et (600–800 °C) = 0.55 eV; 2.5Sr15ErDC–17.25 mS/cm, Et (400–600 °C) = 1.01 eV, Et (600–800 °C) = 0.57 eV; 5Sr15ErDC–16.22 mS/cm, Et (400–600 °C) = 1.05 eV, Et (600–800 °C) = 0.59 eV; 7.5Sr12.5ErDC–15.67 mS/cm, Et (400–600 °C) = 1.03 eV, Et (600–800 °C) = 0.64 eV.

The system $Ce_{0.8}(Sm_{1-x}Sr_x)_{0.2}O_{2-\delta}$ (x = 0.03, 0.5, 0.7) was obtained by the authors of [31]. It was found that the sample $Ce_{0.8}(Sm_{0.7}Sr_{0.3})_{0.2}O_{2-\delta}$ had the highest electrical conductivity, which amounts to 18 mS/cm at a temperature of 700 °C, E_t = 0.86 eV. For the system $Ce_{0.8}Sm_{0.2}O_{2-\delta}$, the electrical conductivity was 12 mS/cm, E_t = 1.05 eV (data were taken from the graphs).

The conductivity of the $Ce_{0.8}Gd_{0.2}O_{2-\delta}$ electrolyte [56] was observed at 16 mS/cm at 700 °C and 0.78 eV activation energy.

4. Discussion

The samples of the ceramics (Y,Ce,Mg,Sr)$O_{2-\delta}$, 10YCe3Mg5Sr, and 10SmCe3Mg5Sr were obtained by the solid-state reaction. It has been shown that the cubic structure of fluorite belonging to CeO_2 prevailed in all systems, but in the (Y,Ce,Mg,Sr)$O_{2-\delta}$ system, the

secondary orthorhombic phase corresponding to SrY_2O_4 was observed, which is due to the poor solubility of Sr^{2+} and Y^{3+} (5–10%) in the cerium oxide lattice.

Microscopy investigations (TEM and REM) showed that each individual powder had a uniform particle size distribution in the nanometer range. The average particle size in (Y,Ce,Mg,Sr)$O_{2-\delta}$, 10YCe3Mg5Sr, and 10SmCe3Mg5Sr compositions was 23.88 nm, 22.32 nm, and 13.4 nm, respectively. After sintering at a temperature of 1500 °C, the grain size increased up to 5.1 μM, 3.95 μM, and 5.07 for (Y,Ce,Mg,Sr)$O_{2-\delta}$, 10YCe3Mg5Sr, and 10SmCe3Mg5Sr, respectively. The obtained SEM images demonstrated the densest structure and the smallest number of pores to be in the 10SmCe3Mg5Sr system. The microhardness and crack resistance measurement results were in a range of 7.07 to 7.3 GPa and 1.48–2.2 $MPam^{1/2}$.

The impedance spectrometry found the lowest activation energy (E_a = 0.62 eV at temperature range 600–800 °C) and the highest value of ionic conductivity (σ_{700} = 20.5 mS/cm) to be in the system 10SmCe3Mg5Sr.

Author Contributions: Conceptualization, I.V.S.; methodology, I.V.S.; validation, I.V.S., A.S.K. and Y.S.N.; formal analysis, Y.S.N.; investigation, I.V.S.; resources, A.S.K.; data curation, I.V.S.; writing—original draft preparation, I.V.S.; writing—review and editing, I.V.S., A.S.K. and Y.S.N.; funding acquisition, A.S.K. and I.V.S. All authors have read and agreed to the published version of the manuscript.

Funding: The work was financially supported by a Program of the Ministry of Education and Science of the Russian Federation for higher education establishments, project No. FZWG-2020-0032 (2019-1569). The work was carried out using the equipment of the Joint Research Center of Belgorod State National Research University «Technology and Materials» with financial support from the Ministry of Science and Higher Education of the Russian Federation within the framework of agreement №075-15-2021-690 (unique identifier for the project RF—-2296.61321X0030).

Informed Consent Statement: Informed consent was obtained from all subjects involved in the study.

Data Availability Statement: The data presented in this study are available on request from the corresponding author.

Conflicts of Interest: The authors declare no conflict of interest.

References

1. Mahmud, L.S.; Muchtar, A.; Somalu, M.R. Challenges in fabricating planar solid oxide fuel cells: A review. *Renew. Sustain. Energy Rev.* **2017**, *72*, 105–116. [CrossRef]
2. Singh, A.; Baredar, P.; Khare, H.; Kumar, A. Fuel cell: Fundamental, classification, application, and environmental impact. In *Low Carbon Energy Supply*; Sharma, A., Shukla, A., Aye, L., Eds.; Springer Nature Singapore: Singapore, 2018; pp. 363–385. Available online: https://link.springer.com/book/10.1007/978-981-10-7326-7 (accessed on 28 June 2022).
3. Jaiswal, N.; Tanwa, K.; Suman, R.; Kumar, D.; Upadhyay, S.; Parkash, O. A brief review on ceria based solid electrolytes for solid oxide fuel cells. *J. Alloys Compd.* **2019**, *781*, 984–1005. [CrossRef]
4. Shen, M.; Ai, F.; Ma, H.; Xu, H.; Zhang, Y. Progress and prospects of reversible solid oxide fuel cell materials. *iScience* **2021**, *24*, 103464. [CrossRef]
5. Leng, Y.J.; Chan, S.H.; Khor, K.A.; Jiang, S.P. Performance evaluation of anode-supported solid oxide fuel cells with thin film YSZ electrolyte. *Int. J. Hydrogen Energy* **2004**, *29*, 1025–1033. [CrossRef]
6. Etsell, T.N.; Flengas, S.N. The electrical properties of solid oxide electrolytes. *Chem. Rev.* **1970**, *70*, 339–376. [CrossRef]
7. Tu, H.; Stimming, U. Advances, aging mechanisms and lifetime in solid-oxide fuel cells. *J. Power Sources* **2004**, *127*, 284–293. [CrossRef]
8. Kharton, V.V.; Marques, F.M.B.; Atkinson, A. Transport properties of solid oxide electrolyte ceramics: A brief review. *Solid State Ion.* **2004**, *174*, 135–149. [CrossRef]
9. Madhusudan, C.; Kasarapu, V.; Chittimadula, M.; Reddy, Y.S.; Reddy, C.V. Synthesis and characterization of Y and Dy co-doped ceria solid electrolytes for IT-SOFCs: A microwave sintering. *Rate Met.* **2021**, *40*, 3329–3336. [CrossRef]
10. Liu, Z.; Ding, D.; Liu, M.; Ding, X.; Chen, D.; Li, X.; Xia, C.; Liu, M. High-performance, ceria-based solid oxide fuel cells fabricated at low temperatures. *J. Power Sources* **2013**, *241*, 454–459. [CrossRef]
11. Ali, A.; Raza, R.; Ullah, M.K.; Rafique, A.; Wang, B.; Zhu, B. Alkaline earth metal and samarium co-doped ceria as efficient electrolytes. *Appl. Phys. Lett.* **2018**, *112*, 43902. [CrossRef]
12. Venkatesh, V.; Redd, C.V. Thermal and electrical properties of Ce0.8-xPrxSm0.2O2-δ electrolyte materials for IT-SOFC application. *Ionics* **2017**, *23*, 3455–3467. [CrossRef]

13. Fu, Y.-P.; Chen, S.-H.; Huang, J.-J. Preparation and characterization of Ce0.8M0.2O2-δ (M = Y, Gd, Sm, Nd, La) solid electrolyte materials for solid oxide fuel cells. *Int. J. Hydrogen Energy* **2010**, *35*, 745–752. [CrossRef]
14. Wu, Y.C.; Lin, C.C. The microstructures and property analysis of aliovalent cations ($Sm^{3+,}$ Mg^{2+}, Ca^{2+}, Sr^{2+}, Ba^{2+}) co-doped ceria-base electrolytes after an aging treatment. *Int. J. Hydrogen Energy* **2014**, *39*, 7988–8001. [CrossRef]
15. Puente-Martínez, D.E.; Díaz-Guillén, J.A.; Montemayor, S.M.; Díaz-Guillén, J.C.; Burciaga-Díaz, O.; Bazaldúa-Medellín, M.E.; Díaz-Guillén, M.R.; Fuentes, A.F. High ionic conductivity in CeO_2 SOFC solid electrolytes; effect of Dy doping on their electrical properties. *Int. J. Hydrogen Energy* **2020**, *45*, 14062–14070. [CrossRef]
16. Ramesh, S. Transport properties of Sm doped CeO_2 ceramics. *Process. Appl. Ceram.* **2021**, *15*, 366–373. [CrossRef]
17. Kang, J.; Feng, W.; Guo, D.; Chen, K.; Gao, S.; Jiang, J.; Lu, C.; Niu, B.; Wang, B. Performance optimization of Ca and Y co-doped CeO_2-based electrolyte for intermediate-temperature solid oxide fuel cells. *J. Alloys Compd.* **2022**, *913*, 165317. [CrossRef]
18. Momin, N.; Manjanna, J.; D'Souza, L.; Aruna, S.T.; Kumar, S.S. Synthesis, structure and ionic conductivity of nanocrystalline $Ce_{1-x}La_xO_{2-\delta}$ as an electrolyte for intermediate temperature solid oxide fuel cells. *J. Alloys Compd.* **2022**, *896*, 163012. [CrossRef]
19. Ihaba, H.; Tagaw, H. Ceria-based solid electrolytes. *Solid State Ion.* **1996**, *83*, 1–16. [CrossRef]
20. Zhang, J.; Lenser, C.; Menzler, N.H.; Guillon, O. Comparison of solid oxide fuel cell (SOFC) electrolyte materials for operation at 500 C. *Solid State Ion.* **2020**, *344*, 115138. [CrossRef]
21. Shao, Z.; Tadé, M.O. *Intermediate-Temperature Solid Oxide Fuel Cells: Materials and Applications, Green Chemistry and Sustainable Technology*; Springer: Berlin/Heidelberg, Germany, 2016.
22. Shannon, R.D. Revised Effective Ionic Radii and Systematic Studies of Interatomic Distances in Halides and Chaleogenides. *Acta Cryst.* **1976**, *32*, 751–767. [CrossRef]
23. Yeh, T.-H.; Chou, C.-C. Ionic conductivity investigation in samarium and strontium co-doped ceria system. *Phys. Scr.* **2007**, *129*, 303–307. [CrossRef]
24. Lubke, S.; Wiemhofer, H.-D. Electronic conductivity of Gd-doped ceria with additional Pr-doping. *Solid State Ion.* **1999**, *117*, 229–243. [CrossRef]
25. Souza, E.C.C. Electrochemical properties of doped ceria electrolyte under reducing atmosphere: Bulk and grain boundary. *J. Electroceram.* **2013**, *31*, 245–253. [CrossRef]
26. Fagg, D.; Pérez-Coll, D.; Núñez, P.; Frade, J.; Shaula, A.; Yaremchenko, A.; Kharton, V. Ceria based mixed conductors with adjusted electronic conductivity in the bulk and/or along grain boundaries. *Solid State Ion.* **2009**, *180*, 896–899. [CrossRef]
27. Dąbrowa, J.; Szymczak, M.; Zajusz, M.; Mikuła, A.; Moździerz, M.; Berent, K.; Wytrwal-Sarna, M.; Bernasik, A.; Stygar, M.; Świerczek, K. Stabilizing fluorite structure in ceria-based high-entropy oxides: Influence of Mo addition on crystal structure and transport properties. *J. Eur. Ceram. Soc.* **2020**, *40*, 5870–5881. [CrossRef]
28. Chen, K.; Pei, X.; Tang, L.; Cheng, H.; Li, Z.; Li, C.; Zhang, X.; An, L. A five-component entropy-stabilized fluorite oxide. *J. Eur. Ceram. Soc.* **2018**, *38*, 4161–4164. [CrossRef]
29. Gild, J.; Samiee, M.; Braun, J.L.; Harrington, T.; Vega, H.; Hopkins, P.E.; Vecchio, K.; Luo, J. High-entropy fluorite oxides. *J. Eur. Ceram. Soc.* **2018**, *38*, 3578–3584. [CrossRef]
30. Wu, Y.-C.; Liao, Y.-Y. Effect of Ca_{2+} and Sr_{2+} doping on the microstructure and cell performance of samaria-doped ceria electrolytes used in solid oxide fuel cells. *Int. J. Hydrogen Energy* **2016**, *41*, 13591–13602. [CrossRef]
31. Ali, S.A.M.; Anwar, M.; Abdalla, A.M.; Somalu, M.R.; Muchtar, A. Ce0.80Sm0.10Ba0.05Er0.05O2-δ multi-doped ceria electrolyte for intermediate temperature solid oxide fuel cells. *Ceram. Int.* **2017**, *43*, 1265–1271. [CrossRef]
32. Gao, Z.; Liu, X.; Bergman, B.; Zhao, Z. Enhanced ionic conductivity of Ce0.8Sm0.2O2-δ by Sr addition. *J. Power Sources* **2018**, *208*, 225–231. [CrossRef]
33. Jaiswal, N.; Kumar, D.; Upadhyay, S.; Parkash, O. Effect of Mg and Sr co-doping on the electrical properties of ceria-based electrolyte materials for intermediate temperature solid oxide fuel cells. *J. Alloys Compd.* **2013**, *577*, 456–462. [CrossRef]
34. Cho, Y.H.; Cho, P.-S.; Auchterlonie, G.; Kim, D.K.; Lee, J.-H.; Kim, D.-Y.; Park, H.-M.; Drennan, J. Enhancement of grain-boundary conduction in gadolinia-doped ceria by the scavenging of highly resistive siliceous phase. *Acta Mater.* **2007**, *55*, 4807–4815. [CrossRef]
35. Preethi, S.; Babu, K.S. Divalent cations modified grain boundary scavenging in samarium doped ceria electrolyte for solid oxide fuel cells. *J. Alloys Compd.* **2019**, *792*, 1068–1078. [CrossRef]
36. Cho, P.-S.; Cho, Y.H.; Park, S.-Y.; Lee, S.B.; Kim, D.-Y.; Park, H.-M.; Auchterlonie, G.; Drennan, J.; Lee, J.-H. Grain-Boundary Conduction in Gadolinia-Doped Ceria: The Effect of SrO Addition. *J. Electrochem. Soc.* **2009**, *156*, B339–B344. [CrossRef]
37. Kumar, S.A.; Kuppusami, P.; Amirthapandian, S.; Fu, Y.-P. Effect of Sm co-doping on structural, mechanical and electrical properties of Gd doped ceria solid electrolytes for intermediate temperature solid oxide fuel cells. *Int. J. Hydrogen Energy* **2020**, *45*, 29690–29704. [CrossRef]
38. Bi, H.; Liu, X.; Zhu, L.; Sun, J.; Yu, S.; Yu, H.; Pei, L. Effect of MgO addition and grain size on the electrical properties of Ce0.9Gd0.1O1.95 electrolyte for IT-SOFCs. *Int. J. Hydrogen Energy* **2017**, *42*, 11735–11744. [CrossRef]
39. Zheng, Y.; Wu, L.; Gu, H.; Gao, L.; Chen, H.; Guo, L. The effect of Sr on the properties of Y-doped ceria electrolyte for IT-SOFCs. *J. Alloys Compd.* **2009**, *486*, 586–589. [CrossRef]
40. Zheng, Y.; Gu, H.; Chen, H.; Gao, L.; Zhu, X.; Guo, L. Effect of Sm and Mg co-doping on the properties of ceria-based electrolyte materials for IT-SOFCs. *Mater. Res. Bull.* **2009**, *44*, 775–779. [CrossRef]

41. Jaiswal, N.; Upadhyay, S.; Kumar, D.; Parkash, O. Sm^{3+} and Sr^{2+} co-doped ceria prepared by citrate–nitrate auto-combustion method. *Int. J. Hydrogen Energy* **2014**, *39*, 543–551. [CrossRef]
42. Zheng, Y.; He, S.; Ge, L.; Zhou, M.; Chen, H.; Guo, L. Effect of Sr on Sm-doped ceria electrolyte. *Int. J. Hydrogen Energy* **2011**, *36*, 5128–5135. [CrossRef]
43. Cioateră, N.; Pârvulescu, V.; Rolle, A.; Vannie, R.N. Effect of strontium addition on europium-doped ceria properties. *Solid State Ion.* **2009**, *180*, 681–687. [CrossRef]
44. Spiridigliozzi, L.; Dell'Agli, G.; Marocco, A.; Accardo, G.; Pansini, M.; Yoon, S.; Ham, H.; Frattini, D. Engineered co-precipitation chemistry with ammonium carbonate for scalable synthesis and sintering of improved Sm0.2Ce0.8O1.90 and Gd0.16Pr0.04Ce0.8O1.90 electrolytes for IT-SOFCs. *J. Ind. Eng. Chem.* **2018**, *59*, 17–27. [CrossRef]
45. Niihara, K.; Morena, R.; Hasselman, D.P.H. Evalution of K1c of brittle solids by the indentation method with low crack-to-indent ration. *Mater. Sci. Lett.* **1982**, *1*, 13–16. [CrossRef]
46. Fu, Y.-P. Ionic conductivity and mechanical properties of Y_2O_3-doped CeO_2 ceramics synthesis by microwave-induced combustion. *Ceram. Int.* **2009**, *35*, 653–659. [CrossRef]
47. Maschio, S.; Sbaizero, O.; Meriani, S. Mechanical Properties in the Ceria-Zirconia System. *J. Eur. Ceram. Soc.* **1992**, *9*, 127–132. [CrossRef]
48. Jaiswal, N.; Singh, N.K.; Kumar, D.; Parkash, O. Effect of strontium (Sr) doping on the conductivity of ceria. *J. Power Sources* **2012**, *202*, 78–84. [CrossRef]
49. Singh, B.; Ghosh, S.; Aich, S.; Roy, B. Low temperature solid oxide electrolytes (LT-SOE): A review. *J. Power Sources* **2017**, *339*, 103–135. [CrossRef]
50. Mogensen, M.; Lybye, D.; Bonanos, N.; Hendriksen, P.V.; Poulsen, F.W. Review. Factors controlling the oxide ion conductivity of fluorite and perovskite structured oxides. *Solid State Ion.* **2004**, *174*, 279–286. [CrossRef]
51. Gerhardt, R.; Nowick, A.S.; Mochel, M.E.; Dumler, I. Grain-Boundary Effect in Ceria Doped with Trivalent Cations: II, Microstructure and Microanalysis. *J. Am. Ceram. Soc.* **1986**, *69*, 647–651. [CrossRef]
52. Kidner, N.J.; Perry, N.H.; Mason, T.O. The Brick Lauer Model Revisited: Introducing the Nanj-Grain Composite Model. *J. Am. Ceram. Soc.* **2008**, *91*, 1733–1746. [CrossRef]
53. Kilner, J.A. Fast oxygen transport in acceptor doped oxides. *Solid State Ion.* **2000**, *129*, 13–23. [CrossRef]
54. Anwar, M.; Ali, S.A.M.; Muchtar, A.; Somalu, M.R. Influence of strontium co-doping on the structural, optical, and electrical properties of erbium-doped ceria electrolyte for intermediate temperature solid oxide fuel cells. *Ceram. Int.* **2019**, *45*, 5627–5636. [CrossRef]
55. Priya, R.; Kaur, S.; Sharma, U.; Pandey, O.P.; Dhoble, S.J. A review on recent progress in rare earth and transition metals activated SrY2O4 phosphors. *J. Mater. Sci. Mater. Electron.* **2020**, *31*, 13011–13027. [CrossRef]
56. Anjaneya, K.C.; Singh, M.P. Synthesis and properties of gadolinium doped ceria electrolyte for IT-SOFCs by EDTA-citrate complexing method. *J. Alloys Compd.* **2017**, *695*, 871–876. [CrossRef]